Direct imaging of intraflagellar-transport turnarounds reveals that motors detach, diffuse, and reattach to opposite-direction trains

Zhiqing Zhang[a,b], Noémie Danné[a,b], Bonno Meddens[a,b], Iddo Heller[a,b], and Erwin J. G. Peterman[a,b,1]

[a]Department of Physics and Astronomy Vrije Universiteit Amsterdam, 1081 HV Amsterdam, The Netherlands; and [b]LaserLaB Amsterdam, Vrije Universiteit Amsterdam, 1081 HV Amsterdam, The Netherlands

Edited by Jonathan M. Scholey, University of California, Davis, CA, and approved September 16, 2021 (received for review August 18, 2021)

Intraflagellar transport (IFT), a bidirectional intracellular transport mechanism in cilia, relies on the cooperation of kinesin-2 and IFT-dynein motors. In *Caenorhabditis elegans* chemosensory cilia, motors undergo rapid turnarounds to effectively work together in driving IFT. Here, we push the envelope of fluorescence imaging to obtain insight into the underlying mechanism of motor turnarounds. We developed an alternating dual-color imaging system that allows simultaneous single-molecule imaging of kinesin-II turnarounds and ensemble imaging of IFT trains. This approach allowed direct visualization of motor detachment and reattachment during turnarounds and accordingly demonstrated that the turnarounds are actually single-motor switching between opposite-direction IFT trains rather than the behaviors of motors moving independently of IFT trains. We further improved the time resolution of single-motor imaging up to 30 ms to zoom into motor turnarounds, revealing diffusion during motor turnarounds, which unveils the mechanism of motor switching trains: detach–diffuse–attach. The subsequent single-molecule analysis of turnarounds unveiled location-dependent diffusion coefficients and diffusion times for both kinesin-2 and IFT-dynein motors. From correlating the diffusion times with IFT train frequencies, we estimated that kinesins tend to attach to the next train passing in the opposite direction. IFT-dynein, however, diffuses longer and lets one or two trains pass before attaching. This might be a direct consequence of the lower diffusion coefficient of the larger IFT-dynein. Our results provide important insights into how motors can cooperate to drive intracellular transport.

intraflagellar transport | motor cooperation | single-molecule imaging | motor turnarounds | diffusion

Almost all eukaryotic cells contain one or multiple cilia, organelles that play crucial roles in sensory perception and signaling (1). The assembly and maintenance of cilia rely on bidirectional intraflagellar transport (IFT) along the cilium, which is mediated by kinesin-2 and IFT-dynein motors (2–8). In *Chlamydomonas*, a single motor, heterotrimeric kinesin-2 (9, 10), drives the anterograde transport of IFT trains, consisting of IFT-particle complexes and IFT motors to the ciliary tip. From the tip, kinesin-2 is passively recycled back to the ciliary base by diffusion, independent of retrograde IFT driven by IFT-dynein (11–15). In *Caenorhabditis elegans* chemosensory cilia, however, two different kinesin-2 motors cooperate to drive anterograde IFT, and they are actively recycled back to the base by IFT-dynein–driven retrograde IFT (5, 9, 16, 17). This marked difference in mode of kinesin returning from tip to base raises the question whether kinesin-2 motors in *C. elegans* are always associated to IFT trains or whether some motors are freely moving around in the cilia. If kinesin-2 motors are always associated with IFT trains, how can they rapidly jump between anterograde and retrograde trains, as inferred in previous studies (18, 19)?

C. elegans chemosensory cilia consist of a cylindrical, microtubule-based axoneme surrounded by a specialized membrane (20). The axoneme emanates from the ciliary base and transition zone to a bipartite structure consisting of the proximal segment and the distal segment made of nine doublet and nine singlet microtubules, respectively (6, 21). IFT is required for proper ciliary biogenesis and maintenance, and IFT requires the cooperation of anterograde kinesin-2 motor proteins (5, 22) and retrograde IFT-dynein motors (8). The core machinery of IFT trains includes kinesin-2 and IFT-dynein motors and a stable IFT-train backbone composed of IFT-A and IFT-B complexes (11) linked by the BBSome (23) to which motors and cargoes can dock and undock (3, 24). IFT trains are assembled in the ciliary base and transported to the ciliary tip by the cooperative action between two types of kinesin-2 motors, heterotrimeric kinesin-II and homodimeric OSM-3 (5, 9, 16, 17). Kinesin-II acts as the "import" motor to drive IFT trains through the base and transition zone toward the proximal segment, possibly avoiding obstacles on the microtubules by sidestepping (25). There, kinesin-II gradually hands over anterograde IFT trains to OSM-3, which drives the long-range transport toward the ciliary tip (18). At the tip, IFT trains are rapidly disassembled and reassembled (14, 26) and transported back to the ciliary base solely by IFT-dynein (8, 15, 27).

Significance

Primary cilia are important organelles that exist in almost all eukaryotic cells. Intraflagellar transport (IFT) is a motor-protein–driven bidirectional intracellular transport mechanism in cilia. Previous studies have shown that motors in *Caenorhabditis elegans* chemosensory cilia undergo rapid turnarounds to effectively work together in driving orderly IFT. The mechanism of motor turnarounds has, however, remained unclear. Here, using a combination of advanced fluorescence imaging and single-molecule analysis, we directly show that the individual turnarounds are due to motors switching between opposite-direction IFT trains. Furthermore, we show that switching events consist of motors detaching from a train, diffusing to another one followed by attachment. This directly demonstrates that motors switch trains by diffusion, which clarifies the mechanism of motor turnarounds.

Author contributions: Z.Z. and E.J.G.P. designed research; Z.Z. performed research; Z.Z., N.D., and B.M. contributed new reagents/analytic tools; Z.Z., N.D., and E.J.G.P. analyzed data; and Z.Z., N.D., I.H., and E.J.G.P. wrote the paper.

The authors declare no competing interest.

This article is a PNAS Direct Submission. J.M.S. is a guest editor invited by the Editorial Board.

[1]To whom correspondence may be addressed. Email: e.j.g.peterman@vu.nl.

This article contains supporting information online at http://www.pnas.org/lookup/suppl/doi:10.1073/pnas.2115089118/-/DCSupplemental.

Published November 3, 2021.

Single-molecule imaging of kinesin-2 and IFT-dynein motors has revealed that motors undergo rapid turnarounds (directional switches) to achieve efficient motor cooperation (18, 19). The anterograde-to-retrograde (a-to-r) turnarounds of kinesin-II and r-to-a turnarounds of OSM-3 in the handover zone (located between 1 and 4 μm from the base) have been interpreted as kinesin-II switching from drivers of anterograde trains to passengers of retrograde trains and OSM-3 switching from passengers of retrograde trains to active drivers of anterograde trains, respectively (18). This handover mechanism is the origin of the efficiency of the cooperation between kinesin-II and OSM-3 because kinesin-II immediately starts to detach from anterograde trains after finishing their function as the import motor while OSM-3 starts to bind to anterograde trains to take over the long-range transport to the tip. Similarly, single-molecule imaging of IFT-dynein has revealed that IFT-dynein can undergo a-to-r turnarounds at all locations along the cilium (19), which has been interpreted as IFT-dynein switching from the deactivated passenger of anterograde trains to the active driver of retrograde trains. Taken together, these single-motor turnarounds are consistent with an overall picture of IFT, in which the IFT-train backbone provides a stable platform, moving from base to tip or back, to which individual motors can rapidly attach and detach during transport, driving effective and regular IFT (3, 18).

So far, however, direct observations of this interpretation that IFT motors switch between opposite-direction trains to turn around have not been made, which leaves a possible alternative explanation, namely that turnarounds are partly due to freely moving motors not associated with IFT trains. To further zoom into the mechanism of IFT motor turnarounds, here we push the envelope of our single-molecule fluorescence imaging capabilities in living *C. elegans*. By applying alternating dual-color imaging, we directly show that during a turnaround, motors switch from one IFT train to another. By increasing our imaging time resolution (up to 30 ms per frame), we show that during the directional switch, motors use diffusion to hop from one train to another.

Results

Simultaneous Imaging of IFT Trains and Motor Turnarounds. To unravel the behavior of single IFT motor proteins switching direction in the context of IFT trains, we implemented a dual-color imaging approach that allows concomitant imaging of individual IFT motor proteins and IFT trains (Fig. 1*A*). We reasoned that using such an approach, the overlay of a single-motor turnaround trajectory with the trajectories of IFT trains would directly reveal whether individual motors are always connected to IFT trains or whether motors can move independently of trains (Fig. 1 *B*, *Left*). The latter case, to the extreme, is the case for kinesin-II in *Chlamydomonas*: here, kinesin-II is not attached to retrograde trains but diffuses back to the base (14, 15). Furthermore, this dual-color approach could also directly show how a motor protein hops from one train to another one moving in the opposite direction: by the direct handover between trains or by a diffusive hop of the motor (Fig. 1 *B*, *Right*).

For dual-color imaging, we here use one strain, XBX-1::eGFP KAP-1::mCherry [expressing enhanced green fluorescent protein (eGFP)-labeled IFT-dynein and mCherry-labeled kinesin-II (19, 28, 29)], with the idea to track one of the labeled motors at the single-molecule level (after reducing the number of active fluorophores by photobleaching) and the other at the train level (limiting photobleaching of this fluorophore as much as possible). We first tried to achieve single-molecule imaging of the eGFP-labeled motor and train imaging using the mCherry-labeled one to make use of the fact that eGFP is more resistant to photobleaching than mCherry (30, 31), which we hoped would result in longer single-molecule trajectories of higher quality. This did not work, however, because the prolonged excitation with 491-nm laser light required to photobleach eGFP to the single-molecule level also excited mCherry (*SI Appendix*, Fig. S1 *A* and *B*), resulting in almost complete photobleaching of mCherry. We then switched to mCherry single-molecule imaging and eGFP train imaging, which resulted in a strong fluorescence background signal in the mCherry channel, caused by the vibronic red tail of the eGFP fluorophore, that overwhelmed the single-molecule mCherry signals (*SI Appendix*, Fig. S1*C*). We succeeded in overcoming this background issue by applying alternating 491/561-nm excitation (see *Materials and Methods* for the implementation), switching laser light every 75 ms using an acousto-optic tunable filter (AOTF) and synchronized imaging with an integration time of 75 ms. In Fig. 1*C* and Movie S1, we show that using this approach, trains (using IFT-dynein as a marker) and single–kinesin-II motors can be tracked simultaneously in living *C. elegans*, clearly revealing a-to-r turnarounds of kinesin-II. A total of 109 of these kinesin-II a-to-r turnarounds were collected in the handover zone together with the motion of IFT trains. The locations of the turnarounds are shown in a histogram in Fig. 1*D* and are consistent with our previous, single-color observation (18).

Colocalization of Individual Kinesin-II Turnarounds with IFT-Train Trajectories. To overlay single–kinesin-II trajectories with the motion of IFT trains, we applied single-molecule tracking (32) on the raw timelapse kinesin-II images to obtain the accurate superresolution trajectories of kinesin-II, from which we recalculated kymographs. These single-motor kymographs were overlaid with kymographs of IFT trains (Fig. 2 *A* and *B*). Kymographs were Fourier filtered in order to separate anterograde and retrograde IFT-train motion (33). From these overlaid single-motor and train kymographs, we calculated the Manders' coefficient M1 (34) to quantify the colocalization coefficient of the trajectories of individual kinesin-II motors with those of IFT trains (Fig. 2*C*). Before, we have applied this correlation approach to quantify the colocalization of IFT-dynein and kinesin-2, both at the train level (19). M1 for anterograde and retrograde motions are both close to 1 (anterograde: M1 = 0.982 ± 0.029, retrograde: M1 = 0.975 ± 0.033, n = 109), indicating that single–kinesin-II trajectories almost always overlay with those of IFT trains (with IFT-dynein as marker). This analysis directly shows that individual kinesin-II motors move together with anterograde IFT trains, most likely as the driver of transport, from base to handover zone, where they fall off the anterograde train and quickly hop on a retrograde train to be transported back to the base as cargo.

In most cases (68 out of 109: 62%; including the one depicted in Fig. 2*B*), a-to-r turnarounds appeared instantaneous. In the rest of the turnarounds (Fig. 2 *D* and *F* and Movie S2) a clear pause could be discerned, lasting longer than three frames (of 150 ms each). Overall, this observation is consistent with our previous observation that directional switches of IFT motors are fast [i.e., on average on the order of the 150-ms integration time (18)]. In 17% of a-to-r turnarounds (18 out of 109), a displacement could be observed in the direction perpendicular to the cilium between anterograde run before the turnaround and retrograde run after (Fig. 2 *E* and *F*). We interpret this offset as a hop of a single kinesin-II from a train moving along a microtubule on one side of the axoneme to another train moving on the other side (perpendicular to the long axis). These perpendicular displacements and pauses observed in part of the kinesin-II turnaround trajectories raise the question: what is the exact mechanism by which individual motors switch from one IFT train to another?

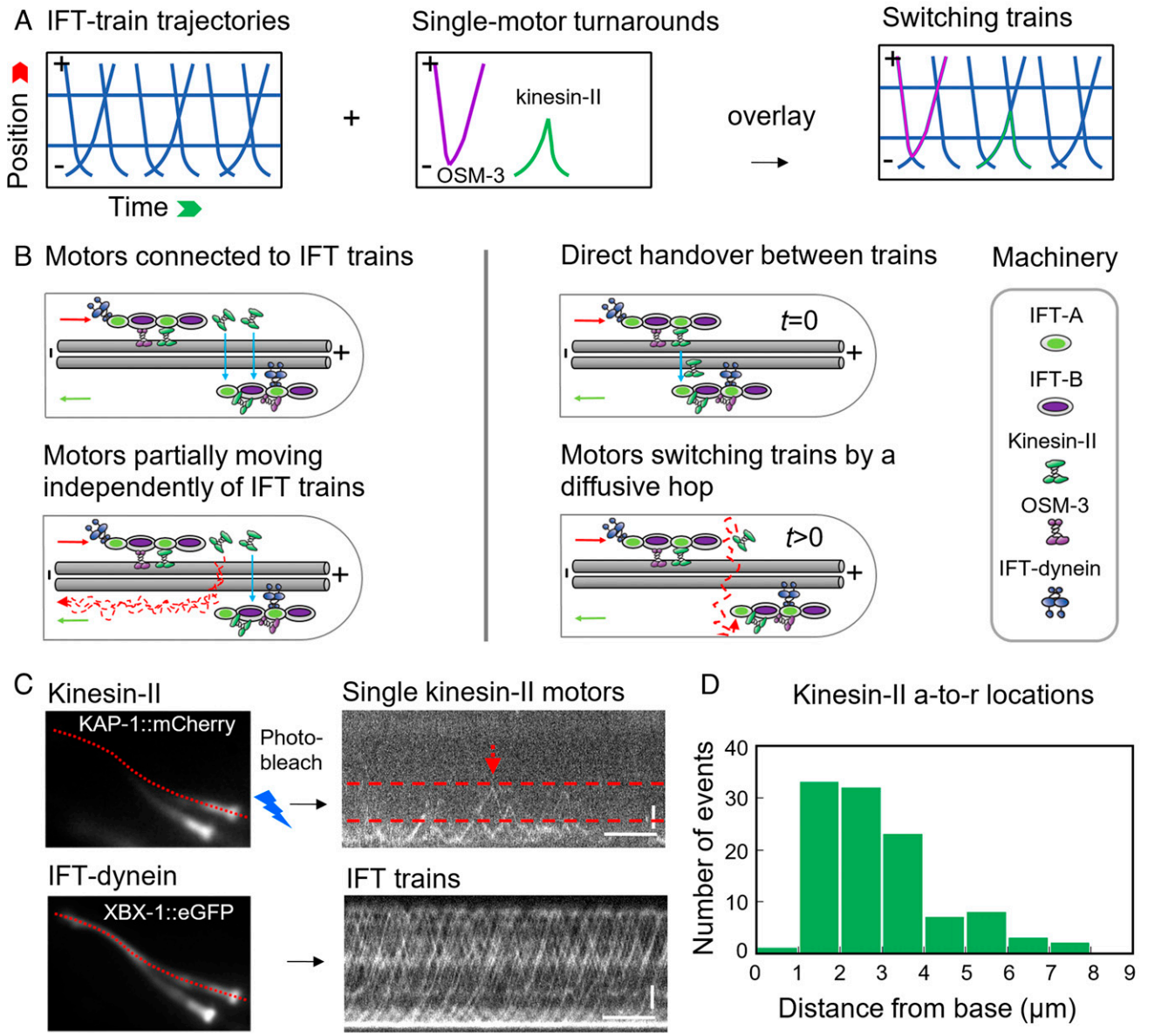

Fig. 1. Alternating dual-color excitation enables simultaneous single-molecule imaging of single-motor turnarounds and IFT-train trajectories. (*A*) Cartoon kymographs depicting the idea of direct visualization of single-molecule motor turnarounds, together with IFT-train trajectories, using simultaneous single-molecule and ensemble imaging. (*B*) Cartoon diagrams depicting kinesin-II a-to-r turnarounds and the models tested in this study. *Left*: are motors (almost) always connected to IFT trains (*Top*), or is there a subset of motors moving independently of trains (*Bottom*), as is the case for kinesin-II in *Chlamydomonas* (which diffuses back from tip to base, disconnected from the IFT machinery)? *Right*: what is the mechanism of motors switching from one train to another? Are motors directly handed over from one train to another (*Top*) without free motion of the motors, or do motors move from train to train in a diffusive hop (*Bottom*)? Red arrow: anterograde train; green arrow: retrograde train; blue arrow: turnaround; red scribble line: diffusion. (*C*) Fluorescence images and kymographs of kinesin-II (KAP-1::mCherry) and IFT-dynein (XBX-1::eGFP) obtained from simultaneous single-molecule imaging of kinesin-II a-to-r turnarounds in the handover zone (between the two red dashed lines) and ensemble imaging of IFT trains represented by IFT-dynein. See Movie S1 for the turnaround event indicated by the red arrow (horizontal scale bar, 10 s; vertical scale bar: 1 μm). (*D*) Histogram of the locations of kinesin-II a-to-r turnarounds (n = 109 single motors pooled from 51 worms, 59 cilia).

Fast Single-Molecule Imaging Reveals How Individual Motors Switch Trains: Detach–Diffuse–Attach. To get a deeper insight in the mechanism by which IFT motors switch between opposite-direction trains, we performed single-molecule imaging in living *C. elegans* on strains expressing KAP-1::eGFP or OSM-3::paGFP (photoactivatable green fluorescent protein) with a higher time resolution. To this end, we decreased the camera frame integration time from 150 to 30 ms for eGFP-tagged motors (Fig. 3 *A*–*C*) and 50 ms for paGFP-tagged motors (Fig. 3*D*), resulting in surprisingly more-detailed single-molecule trajectories. In kymographs of kinesin-II (KAP-1::eGFP) a-to-r (Fig. 3*A*, Movie S3, and *SI Appendix*, Fig. S2*A*) and r-to-a turnarounds (Fig. 3*B*, Movie S4, and *SI Appendix*, Fig. S2*A*), we observed jagged, fluctuating kymograph tracks sandwiched between straight tracks of opposite direction, indicating that individual kinesin-II motors diffuse through the cilium after detaching from a moving IFT train until reattaching to another, opposite-direction–moving one. We also observed this diffusion behavior between subsequent bouts of same-direction motion (r-to-r, Fig. 3*B* and Movie S4; a-to-a, Fig. 3*C* and Movie S5), indicating that

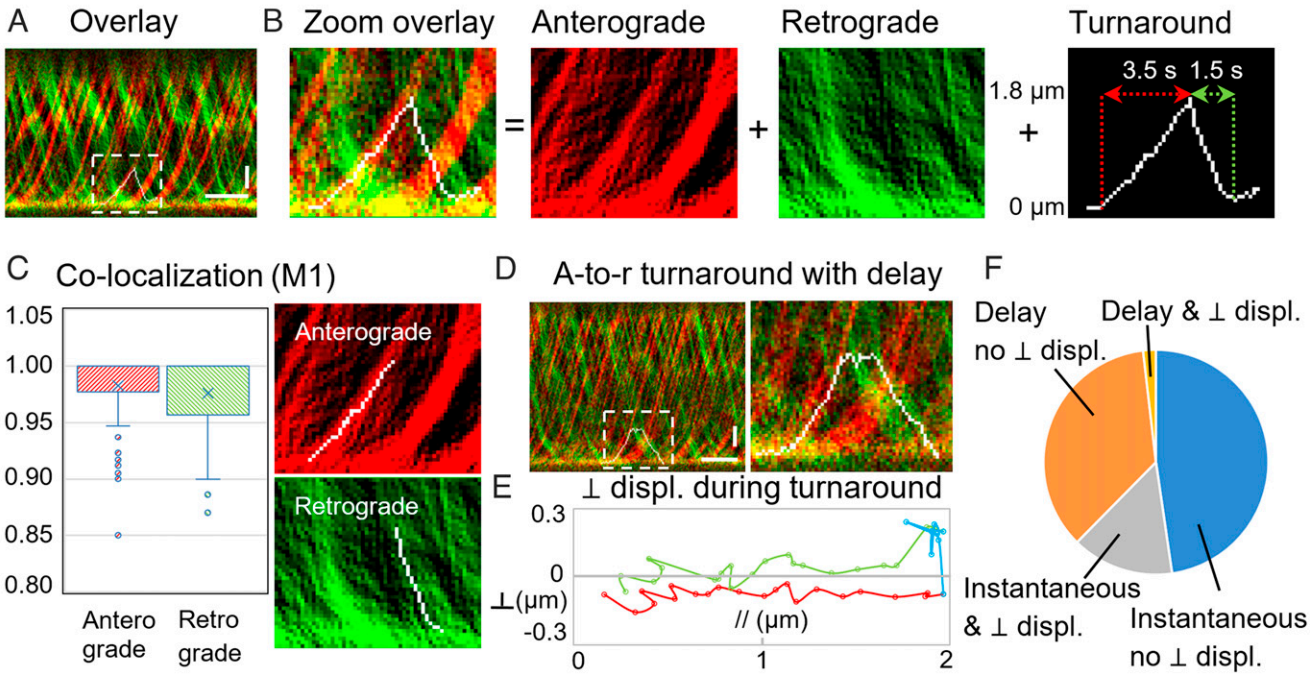

Fig. 2. Colocalization of single-molecule kinesin-II turnarounds with IFT-train motion provides direct evidence of motors switching from one train to another in the handover zone (horizontal scale bar, 5 s; vertical scale bar, 1 µm). (*A* and *B*) Overlaid and expanded kymographs of a single-molecule kinesin-II turnaround and the IFT-train trajectories (color-coded for direction), showing that kinesin-II switches from an anterograde train to a retrograde train, without time delay. (*C*) Manders' colocalization analysis shows a high degree of colocalization of kinesin-II anterograde and retrograde motion with IFT-train trajectories. (*D* and *E*) Example of a single-molecule kinesin-II turnaround that shows delayed docking to a retrograde train (*D* and Movie S2) and anterograde (red, *E*) and retrograde (green, *E*) trajectories that are not overlapping in space because of a displacement in the perpendicular direction during the turnaround (blue, *E*). (*F*) Quantification of all turnarounds identified (n = 109 single motors pooled from 51 worms, 59 cilia): 47.7% (n = 52) turnarounds were instantaneous without perpendicular displacement (blue), 14.7% (n = 16) were instantaneous turnarounds with perpendicular displacement (gray), 35.8% (n = 39) were turnarounds with a delay without perpendicular displacement (orange), and 1.8% (n = 2) were turnarounds with a delay showing perpendicular displacement (yellow). ⊥ displ., perpendicular displacement.

an individual kinesin-II motor can reattach to IFT trains moving in the same direction as the one it has just detached from. Similar observations were made for OSM-3 (OSM-3::paGFP; Fig. 3*D*, Movie S6, and *SI Appendix*, Fig. S2*B*). The locations in the cilia where kinesin-II undergoes a-to-r and OSM-3 undergoes r-to-a turnarounds are consistent with earlier observations recorded with a frame integration time of 150 ms (18) (Fig. 3 *E* and *F*). We next looked into the turnaround behavior of IFT-dynein. In an earlier study (19), we have shown that IFT-dynein can undergo a-to-r turnarounds at all locations along the cilium, switching from being a cargo on a kinesin-2–driven anterograde train to an active driver of a retrograde train. Fast single-molecule imaging of IFT-dynein (XBX-1::eGFP) revealed that this motor also diffuses during a-to-r (Fig. 3*G* and Movie S7) and other train switches (*SI Appendix*, Fig. S2*C*). The locations of a-to-r turnarounds (Fig. 3*H*) were consistent with the previous (lower time resolution) study (19), but here we managed to image the cilia in focus over a longer extent of their length, from base to far into the distal segment (although the tip was not always perfectly in focus). This revealed an expected a-to-r turnaround "hotspot" close to the distal tip that was not discerned in our previous study. The locations of a-to-r turnarounds of OSM-3 (*SI Appendix*, Fig. S2*D*) were similar and consistent with our earlier study (18). Taken together, these fast single-motor measurements indicate that all three IFT motors in *C. elegans* chemosensory cilia diffuse after detachment from one IFT train before reattaching to another.

Analysis of Single-Molecule Trajectories Reveals Location-Dependent Diffusion Behavior. To further characterize and quantify the diffusion behavior, we extracted single-molecule trajectories from the original image sequences of all three IFT motors with single-particle tracking using the Fiji/ImageJ (35) plugin Trackmate (32). A spline was drawn along the cilium to define a local coordinate system with the x-coordinate reflecting position along the cilium and the y-coordinate perpendicular to the cilium. In Fig. 4*A*, an example trajectory of the position along the cilium of a kinesin-II motor making an a-to-r turnaround is shown. We next characterized the trajectories with mean-square displacement (MSD) analysis (36–39). To this end, we calculated the MSDs within a moving time window (40 frames [1.2 s in total] for kinesin-II and IFT-dynein and 30 frames [1.5 s in total] for OSM-3) along the trajectory and determined, for each time window, the generalized transport coefficient γ and the exponent α using the formula $MSD(\tau) = \gamma\tau^{\alpha}$ (with τ the time lag) (40) (Fig. 4*A*). α values usually range between 0 and 2, where $\alpha = 0$ signifies static particles, $0 < \alpha < 1$, subdiffusion, which can be caused by confinement, $\alpha = 1$ normal, free diffusion, and $\alpha = 2$ directed motion, driven by active transport. γ values represent the amplitude of the underlying motion and can be used to calculate velocity in case of directed motion or diffusion constant in case of diffusive motion. We used thresholds in the α and γ trajectories to identify bouts of active transport (threshold $\alpha > 1 + \sigma$, $\sigma = -0.05$, 0, 0.1 for kinesin-II, OSM-3, and IFT-dynein, respectively), free diffusion (threshold $\alpha \leq 1 + \sigma$ and $\gamma > 0.1\ \mu m^2.s^{-\alpha}$), and subdiffusion (threshold $\alpha \leq 1 + \sigma$ and $\gamma \leq 0.1\ \mu m^2.s^{-\alpha}$) within trajectories (Fig. 4 *A* and *B*). We performed this analysis on single-molecule trajectories showing turnarounds of kinesin-II, OSM-3, and IFT-dynein (see *SI Appendix*, Fig. S3 for examples of the latter two motors) and found that the MSD approach identified bouts of diffusion during turnarounds in 30% of kinesin-II (61 out of 201), 44% of OSM-3 (50 out of 113), and 64% of IFT-dynein trajectories

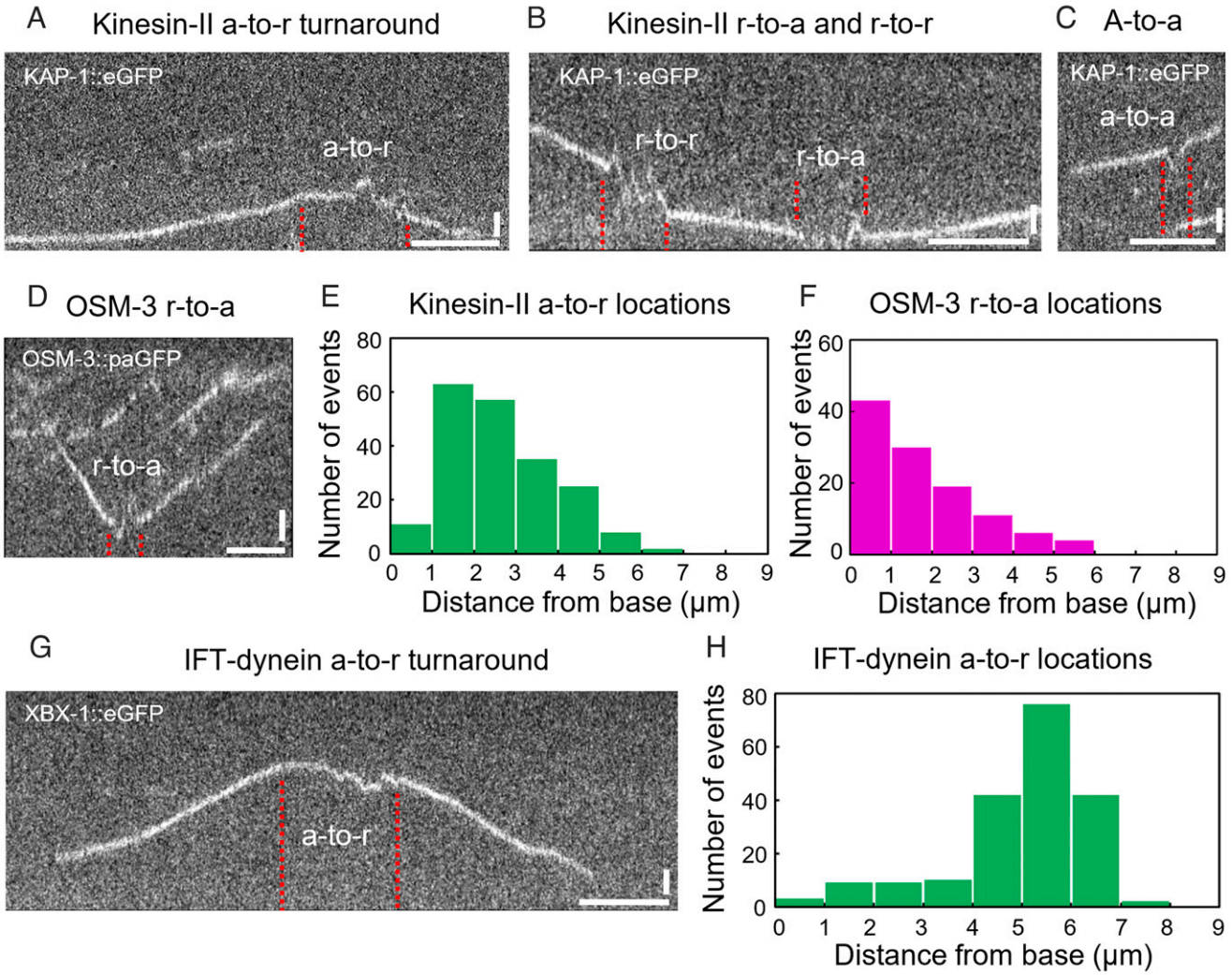

Fig. 3. Fast single-molecule imaging of kinesin-2 and IFT-dynein reveals that "detach–diffuse–attach" is the mechanism by which individual motors switch trains. Red dashed lines indicate the time intervals at which a single motor diffuses from one IFT train to another (horizontal scale bar, 2 s; vertical scale bar, 1 μm). (*A–C*) Representative kymographs of kinesin-II a-to-r, r-to-a, r-to-r, and a-to-a train switches, with frame integration time 30 ms, showing clear signs of diffusion during the switch. (*D*) Representative kymograph of OSM-3 r-to-a turnarounds, with frame integration time 50 ms, showing clear signs of diffusion during the turnaround. (*E*) The locations of kinesin-II a-to-r turnarounds (n = 201 single molecules pooled from 36 worms, 51 phasmid cilia). (*F*) The locations of OSM-3 r-to-a turnarounds (n = 113 single molecules pooled from 40 worms, 49 phasmid cilia). (*G*) Representative kymograph of IFT-dynein a-to-r turnarounds, showing diffusion during turnarounds with frame integration time 30 ms. (*H*) Locations of IFT-dynein a-to-r turnarounds (n = 193 single molecules pooled from 35 worms, 48 phasmid cilia).

(124 out of 193), confirming that all three motors, after detaching from one train, diffuse to another one, to which they reattach.

We next determined the instantaneous diffusion coefficients (41) as a function of location in the cilium (Fig. 4*C*). We did this instead of using the γ-based generalized diffusion coefficients in order to fix the units of the diffusion coefficients to $\mu m^2/s$ (*Materials and Methods*). The diffusion coefficient along the ciliary long axis mostly increased for all three motors going from base and transition zone to the proximal segment, reaching a maximum in the middle of the proximal segment, after which it decreased again (Fig. 4*C*). The lower diffusion coefficient in base and transition zone might be due to the dense structures there [e.g., the transition fibers and the so-called ciliary necklace at the base and the Y-shaped linker proteins in the transition zone (42, 43)]. Furthermore, electron-microscopy and superresolution fluorescence microscopy studies have revealed that the cilium is widest (~300 nm) roughly halfway the proximal segment (44, 45), which might provide the motors more space to diffuse freely, while it is narrowest (~100 nm) in the distal segment. In addition, we found that the diffusion coefficient of OSM-3 (maximum value 0.30 $\mu m^2/s$) was slightly higher than that of kinesin-II (maximum value 0.22 $\mu m^2/s$). At this point, we cannot exclude that this small difference is caused by the different integration times used for the two motors. The diffusion coefficient of IFT-dynein we obtained (maximum value 0.10 $\mu m^2/s$) was substantially lower than those of the kinesin-2 motors, which is consistent with the molecular mass of IFT-dynein being almost five times larger than those of the kinesin-2 motors (~1.4 versus ~0.3 MDa) (11, 16, 46, 47). The diffusion coefficient in the direction perpendicular to the ciliary long axis was much smaller than parallel (1:10), which is most likely limited by the localization accuracy.

The Location-Dependent Diffusion Time. We next used the MSD analysis to determine the diffusion times of kinesin-II a-to-r, OSM-3 r-to-a, and IFT-dynein a-to-r turnarounds. We define diffusion times as the times taken for individual motors to diffuse between opposite-direction IFT trains (Fig. 4 *A* and *B*).

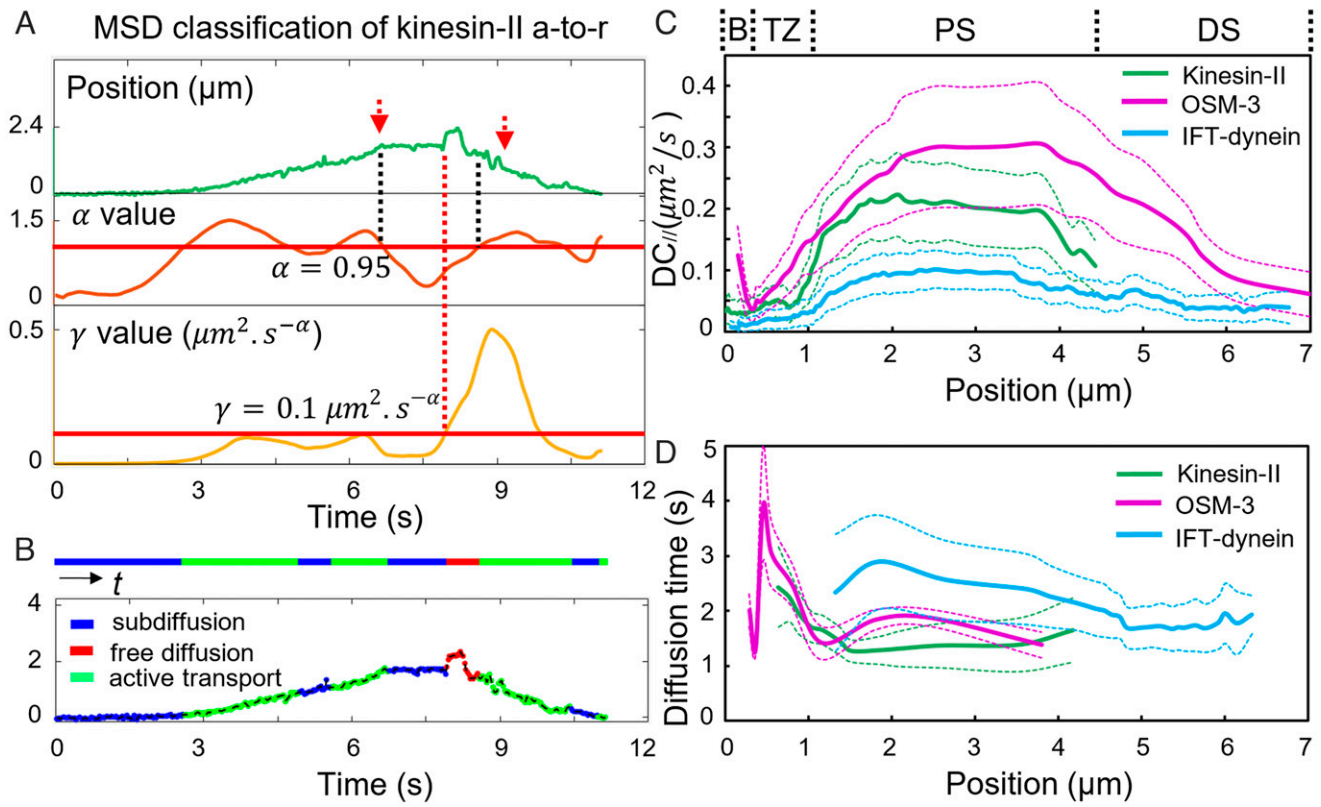

Fig. 4. Single-molecule tracking and analysis with MSD. (*A*) Representative single-molecule trajectory obtained from single-molecule tracking (same data as shown in Fig. 3*A*) and the MSD analysis yielding α and γ values. The red arrows in the trajectory indicate a diffusion interval as identified by a human observer. The black dashed lines indicate a diffusion interval as revealed by MSD analysis, using a threshold of $\alpha = 0.95$. The red dashed line indicates further distinction between subdiffusion and free diffusion by applying an additional threshold of $\gamma = 0.1\ \mu m^2.s^{-\alpha}$. (*B*) Identification of intervals of subdiffusion, free diffusion, and active transport in the trajectory of *A*, identified by MSD classification using the thresholds $\alpha = 0.95$ and $\gamma = 0.1\ \mu m^2.s^{-\alpha}$. (*C*) The location-dependent instantaneous diffusion coefficient (DC) of the three motors. Solid lines indicate the averaged DC over ~15 points, and dashed lines represent mean ± SEM. B, base; TZ, transition zone; PS, proximal segment; DS, distal segment. (*D*) The location-dependent diffusion times of the three motors, excluding direct turnarounds. Solid lines indicate the averaged diffusion time over five points, and dashed lines represent mean ± SEM.

Diffusion times of kinesin-II and OSM-3 in the handover zone (located between 1 and 4 μm from the base) were similar, 1.3 ± 0.1 and 1.7 ± 0.1 s, respectively (Fig. 4*D*). Taking also into account the direct turnaround events (setting their diffusion times to 0 s) resulted in average diffusion times of 0.3 and 0.5 s for kinesin-II and OSM-3, respectively (*SI Appendix*, Fig. S4). These rather short diffusion times explain why we did not observe clear evidence for diffusion in our previous study with a frame integration time of 150 ms (18). For both kinesins, the diffusion time was relatively longer in transition zone and base, ~2.5 s (excluding direct turnarounds), most likely due to the lower diffusion coefficient and the confining effect of the structural proteins here, which can keep diffusing motors longer away from moving trains. We identified too few kinesin turnaround events in the distal segment to reliably determine the diffusion time there. The diffusion time of IFT-dynein in the proximal segment [~2.6 ± 0.3 s excluding direct turnarounds (Fig. 4*D*) and 1.8 s including direct turnarounds (*SI Appendix*, Fig. S4)] was about double that of the kinesins and decreased slightly toward the distal segment. The lower diffusion time in the distal segment might be due to the smaller diameter of the cilium here, keeping IFT-dynein closer to the microtubule track and the IFT trains moving along the microtubules, potentially enhancing the probability of an IFT-dynein reattaching to an IFT train.

Discussion

Previous studies have reported that IFT motors undergo rapid turnarounds in *C. elegans* chemosensory cilia to hand over cargo to other motors in order to achieve efficient motor cooperation (18, 19). It had, however, not been possible to directly visualize how motor proteins turn around. It thus has remained unclear what the underlying mechanism is by which individual motors switch direction without affecting the directionality of IFT in *C. elegans* cilia. Here, we improved our fluorescence imaging capabilities to provide insights into motor turnarounds. We find that 1) the turnarounds are actually single motors switching between IFT trains moving in the opposite direction; 2) the process of switching trains can be dissected into three consecutive steps: detach, diffuse, and attach; 3) when motors are not associated to IFT trains, they are free to diffuse, and the diffusion coefficient is dependent on the ciliary location and structure; and 4) the diffusion time, or the time needed for individual motors to switch trains, is also location dependent.

We have directly shown, using dual-color imaging, that the turnarounds are indeed motors switching between opposite-direction IFT trains rather than the behaviors of motors moving independently of IFT trains. The trajectories obtained show that the switching process can be dissected into detachment and attachment and provide accurate information on where and when detachment and attachment take place. Moreover, the observation of turnarounds with a delay between detachment and attachment or perpendicular displacements triggered us to subsequently study how motors can switch between IFT trains moving in opposite direction. For this, however, a much-higher time resolution was needed, which was not possible with single-molecule imaging of mCherry in the dual-color scheme

because of its limited photostability. To obtain a higher time resolution, we performed fast single-molecule imaging using only the more stable eGFP or paGFP, and we obtained a three to fivefold improvement of the time resolution compared to previous studies. In the future, the time resolution might be pushed further by using brighter fluorescent reporters such as mNeonGreen (48) or using other imaging methods such as Hessian structured illumination microscopy (25) with multiple copies of fluorescent proteins tagged to one motor. The three to fivefold improvement of the time resolution we obtained here is, however, sufficient to reveal that individual motors switch between IFT trains via a detach–diffuse–attach mechanism, directly exposing that diffusion is an intrinsic part of the motor turnaround process.

In *C. elegans* cilia, motors were thought to be associated with IFT trains most of the time (3, 18). Our study has refined this picture, revealing that motors are detached from IFT trains for a short while when switching from one train to another. In these intervals, they are free to diffuse with diffusion coefficients of ~0.2 $\mu m^2/s$ for kinesin-II, ~0.3 $\mu m^2/s$ for OSM-3, and ~0.1 $\mu m^2/s$ for IFT-dynein in the proximal segment. In the primary cilia of cultured mammalian cells, similar diffusion coefficients have been reported for transmembrane proteins: ~0.25 $\mu m^2/s$ for SSTR3 (49), ~0.26 $\mu m^2/s$ for Smoothened (50), and ~0.1 $\mu m^2/s$ for PTCH1 (51). Diffusion coefficients reported for nonmembrane-associated proteins in cilia are substantially higher: 1.68 $\mu m^2/s$ for kinesin-II in *Chlamydomonas reinhardtii* flagella (14), and 3.6 and 0.69 $\mu m^2/s$, respectively, for GFP and FKBP (YFP-FKBP-ΔN β-Gal,) in the primary cilia of NIH3T3 cells (52, 53). These comparisons indicate that diffusion coefficients of ciliary proteins vary substantially between organisms and ciliary substructure. In line with this, we have found in *C. elegans* that the diffusion coefficients of motor proteins are dependent on the location within the cilium, potentially reflecting local ciliary structure and diameter. For example, kinesin-2 motors show a ~5 times lower diffusion coefficient at the ciliary base than in the proximal segment, which is in line with previous studies that have shown that the base and transition zone act as a diffusion barrier for proteins above 60 kDa (42). In *Chlamydomonas*, it has been shown that the diffusion coefficient of kinesin-II plays an important role in ciliary length control (54). Our data suggest that in *C. elegans*, the diffusion coefficients of free motor proteins affect the efficiency of the motors' switching between trains. Namely, in the proximal segment we observed higher diffusion coefficients for the kinesins, correlated with substantially shorter diffusion times compared to base and transition zone. We note, however, that such a correlation is less evident in our data for IFT-dynein, which has a diffusion coefficient in the proximal segment that is about twice that in the distal segment, while the diffusion time is also higher. A key difference between *Chlamydomonas* and *C. elegans* IFT is that in *Chlamydomonas*, kinesins-2 diffuses back from tip to base, while in *C. elegans* the kinesin motors are actively transported by IFT-dynein (3). It could thus very well be that in both organisms, kinesin diffusion coefficients play a key role in IFT regulation: in *Chlamydomonas* directly, by governing the time it takes the kinesins to diffuse back to the base, in *C. elegans* a bit more indirectly, by governing the time it takes the kinesins to connect to an opposite-direction IFT train.

We have shown that motors detach from a moving IFT train, diffuse for a while, and then reattach to another train with "free seats" either moving in the opposite or the same directions. This suggests that the diffusion time depends on the time that a motor encounters another train, which is governed by the diffusion coefficient of the free motors and the frequency of anterograde and retrograde trains. This could explain why the diffusion time of IFT-dynein in the distal segment is shorter than in the proximal segment, while the diffusion constant is also lower, namely because the frequency of retrograde trains in the distal segment is ~20% higher than in the proximal segment [as estimated from IFT-dynein flux (19)]. To get insight into the efficiency of motors reattaching to trains, we compare the diffusion times we obtained (0.3 s for kinesin-II, 0.5 s for OSM-3, and 1.8 s for IFT-dynein in the proximal segment, taking into account all turnarounds including direct ones) to IFT-train frequencies obtained before [0.8 anterograde trains/s and 1.3 retrograde trains/s (19)]. These comparisons indicate that, on average, the kinesins let less than one opposite-direction train pass before reattaching, while IFT-dynein lets more than two trains pass. This difference could be the consequence of the higher diffusion coefficients of the kinesins compared to IFT-dynein. In addition, the kinesins could have a higher affinity for IFT trains than IFT-dynein. Taken together, this reveals that the diffusive hops of in particular the kinesins are remarkably efficient, which enables the tight regulation of motor handover in the proximal segment. This motor handover is a key aspect of IFT in *C. elegans* chemosensory cilia, which requires the finely orchestrated cooperation of kinesin-II and OSM-3 to be efficient (18).

We note that during turnarounds, individual motors switch between three different states: 1) connected to IFT particles and active in driving transport ("drivers"); 2) disconnected from IFT particles and microtubules, inactive, and diffusing around; and 3) connected to IFT particles and inactive cargo ("passengers"). Recent in vitro reconstitution studies have indicated that OSM-3 binding to IFT-B complexes is mediated by IFT70 (DYF-1), which fully activates the motor (55). This might be equivalent to state 1. Earlier experiments have been shown that OSM-3 is autoinhibited and does not bind to microtubules when no cargo is bound (56), which might be the case in state 2. An interesting question is what the nature is of state 3. Is IFT70 (DYF-1) also involved in OSM-3 binding to retrograde trains and its inactivation? An alternative could be that inactive OSM-3 interacts with retrograde trains mediated by other IFT-particle proteins.

Previous studies mostly viewed motor detachment and attachment as an integral step regulated by the same factors. Male germ cell–associated kinase DYF-5 and cell cycle–related kinase DYF-18 have been reported to regulate the undocking/docking of kinesin-2 motors and the handover between them (57–60) by affecting motor distribution, IFT train velocity, and/or IFT train frequency. It is, however, not clear how these kinases are involved in the process of detachment and/or attachment. We have shown here that detachment and attachment are separate steps, suggesting that they may be regulated by different factors and that DYF-5/DYF-18 kinases might only regulate the detachment. To shed further light on this, deeper insight in the ratio between a-to-r turnarounds and a-to-a switches might be useful (as well as between r-to-a turnarounds and r-to-r switches). This ratio is, however, difficult to obtain in an unbiased way because the same-direction switches are much harder to identify (Fig. 3*C*). Single-molecule imaging of the kinesin-2 motors in mutant worms lacking DYF-5 or DYF-18 function might reveal important insights in the effect of these kinases on motor regulation.

In conclusion, we have presented major improvements in our approaches to image single-motor proteins in living *C. elegans.* Using these methods, we have revealed how IFT motor proteins switch trains and thus provided important insights into the mechanism by which different motor proteins cooperate to drive intracellular transport.

Materials and Methods

***C. elegans* Strains.** The *C. elegans* strains used in this study are listed in *SI Appendix*, Table S1. All the strains were constructed with MosSCI (18, 61),

carrying integrated single-copy transgenes encoding for fluorescently labeled IFT components. Worm maintenance and genetic crosses were performed with standard *C. elegans* techniques (62). Nematodes were grown at 20 °C on Nematode Growth Medium plates that were seeded with *Escherichia coli* HB101 bacteria.

Fluorescence Microscopy and Alternating Dual-Color Illumination. Fluorescence images were generated using a custom-built episcopic-illuminated wide-field fluorescence microscope described in detail in Prevo et al. (18) by adding an additional alternating illumination module (*SI Appendix*, Fig. S5). Briefly, the fluorescence microscope was operated by a Micro-Manager software interface, built around an inverted microscope body fitted with a 100× oil-immersion objective. Two excitation beams, provided by two diode-pumped solid-state lasers, were combined and passed through an AOTF for wavelength selection and intensity control. The combined beams went through a quarter-wave plate to obtain circular polarization and through a diffuser to obtain uniform illumination before being coupled into the objective using a dichroic mirror. The emission light was collected by the objective and directed into a two-way image splitter. There, the light was separated into two beams using a dichroic longpass filter, and the two beams were filtered by emission filters, which were finally projected side by side onto an electron-multiplying charge-coupled device (EMCCD) camera. One emission light path was blocked for single-color imaging. Additional 1.5× (inside Eclipse Ti) and 2× (inside the image splitter) intermediate magnification resulted in one camera pixel corresponding to 53 × 53 nm in the image plane.

In the alternating dual-color imaging experiment, an additional module was added to achieve the alternating dual-color excitation. An Arduino-compatible board (Adafruit ItsyBitsy M4) was used as a digital-to-analog converter to connect the camera to the AOTF module (AOTF plus its driver Multi Digital Synthesizer), which enabled the communication between camera and AOTF (*SI Appendix*, Fig. S5*A*). The goal of using this Arduino-compatible board was to split one camera frame with 150-ms integration time into two frames with 75-ms integration time, one with only 491-nm excitation and the other with only 561-nm excitation (*SI Appendix*, Fig. S5*B*). This goal was achieved from two observations: 1) the camera has a digital output and it generates a digital output signal when an image scan is completed and 2) the AOTF can switch on and off the selected laser lights at very high frequency, but it acquires an analog signal input to achieve wavelength control and laser intensity control. Based on these two observations, we set the integration time of the camera to 75 ms, and thus the camera generated a digital signal every 75 ms. The Arduino-compatible board was used to convert the digital signal from the camera to an analog signal which was sent to the AOTF for switching one laser beam on and the other off. The amplitude of the analog signal can be set in the Micro-Manager for the laser intensity control via the AOTF, and an open-source plugin was developed in our group as a device adaptor of Micro-Manager (https://micro-manager.org/wiki/Arduino32bitBoards). By using this alternating illumination module, each time resolution (150 ms) of imaging was split into two equal parts, one used for eGFP excitation and the other used for mCherry excitation. Note that the time resolution for each channel stayed 150 ms.

Imaging Preparation and Recording. We used a modified version of Brust-Mascher et al. (63) for the preparation of fluorescence imaging in living *C. elegans* hermaphrodite worms. Young adult hermaphrodites were anesthetized in 5 mM levamisole in M9 at room temperature (20 °C), and they were immobilized on a 2% agarose in M9 pad, which was covered with a 22 × 22-mm cover glass and sealed with VaLaP to prevent media evaporation. Then samples were placed on the inverted microscope and imaged at room temperature. Fluorescence images were recorded at 150 ms per frame in the beginning to localize the phasmid cilia at the tail of *C. elegans*. We selected the cilia with their base, proximal segment, and most of distal segment (except for the ciliary tip) in focus for ensemble and single-molecule imaging. After focusing on the cilia in the tail, the frame rate of imaging was set to 75 ms in the alternating dual-color imaging experiment and to 30/50 ms in the fast single-molecule imaging experiment.

Image Analysis. After imaging, kymographs were generated by the open-source tool KymographClear that was previously developed in our laboratory as a Fiji/ImageJ plugin (33). This tool uses subpixel interpolation, resulting in a more-detailed curve based on a user-drawn spline. Furthermore, it allows for intensity averaging around the curve to generate clearer kymographs (*SI Appendix*, Fig. S6). In addition, Fourier filtering was implemented to separate three different motility components (forward moving, backward moving, and static) into separate kymographs, which also slightly enhanced the visibility of the separated motions (*SI Appendix*, Fig. S7). For the single-molecule time-lapse data, we used the Trackmate plugin in Fiji (32) to extract their Euclidean coordinates of single-molecule trajectories and link trajectories. In a first step, this approach makes use of a Laplacian of Gaussian filter to detect particles in the timelapse data, greatly enhancing the visibility of fluorescent spots in the data (*SI Appendix*, Fig. S8). To convert the Euclidean coordinates into the long and perpendicular axis coordinates of a cilium, a spline was drawn along the cilium to define the *x*-axis of displacement, and *y*-coordinates are perpendicular to the spline. In the alternating dual-color experiment, the *x*-coordinates of the single-molecule trajectories of kinesin-II were used to replot the kymographs, which were overlaid with the kymographs of IFT trains.

The single-molecule trajectories of turnarounds, obtained from the fast single-molecule imaging experiment (Datasets S1–S3), were further analyzed using a sliding window variant (64) of MSD analysis (40), using a window of 40 frames (1.2 s) for kinesin-II and IFT-dynein and 30 frames (1.5 s) for OSM-3. We used an α-value–based approach to classify the data points on the trajectories; that is, the points with α-values less than $1+\sigma$ ($\sigma = -0.05,\ 0,\ 0.1$ for kinesin-II, OSM-3, and IFT-dynein, respectively) were classified as diffusion and others as active transport. The window width and threshold values were chosen on basis of simulations of diffusive and directed motion with parameters (velocity, diffusion coefficient, integration time, and localization inaccuracy) equal to the experiments. A turnaround event was classified as diffusive if a diffusion event was detected by the MSD analysis during the turnaround. The turnaround location was determined according to the maximal or minimal displacement of a trajectory. To achieve a unified comparison of different diffusion events, we selected the Holcman approach (41) to compute the instantaneous diffusion coefficient of a diffusion event instead of the standard γ-value–based approach. The instantaneous diffusion coefficient was extracted from the slope of the graph showing the instantaneous MSD in function of the time lags ($n.dt$) $-$ $MSD(n.dt) = (x(t+n.dt) - x(t))^2$, where $n = 1, 2, 3$, dt is the time between two frames, and $x(t)$ is the position at the time t. We have taken into account the effect of the localization inaccuracy (~50 nm) on the diffusion coefficients when this method was implemented. After MSD analysis, the diffusion time of a diffusion event was computed from the number of frames showing diffusion. The parameters of diffusion and active transport obtained from MSD analysis are listed in *SI Appendix*, Table S2.

Manders' Colocalization Coefficients. In the alternating dual-color imaging data, the eGFP and mCherry channels were aligned after imaging by aligning the ciliary base that was clearly visible in both channels. The same spline was used to generate the kymographs for both channels. The Manders' coefficient M1 was generated, by using the Coloc2 plugin in Fiji (34, 35), to measure how precise the anterograde and retrograde trajectories of individual kinesin-II motors (the mCherry channel) were localized with those of IFT trains (the eGFP channel) by drawing a region of interest containing the anterograde or retrograde trajectories of kinesin-II.

Data Availability. All study data are included in the article and/or supporting information.

ACKNOWLEDGMENTS. We thank the members of our "worm team" (Aniruddha Mitra, Christine Bruggeman, Jaap van Krugten, Elizaveta Loseva and Wouter Mul) for discussion of experiments and analysis, in particular the discussions with Aniruddha Mitra that resulted in the idea to try the single-molecule imaging with improved time resolution. We acknowledge financial support from the European Research Council under the European Union's Horizon 2020 research and innovation programme [E.J.G.P.; Grant Agreement No. 788363 "How intraflagellar transport shapes the cilium: a single-molecule systems study" (HITSCIL)].

1. V. Singla, J. F. Reiter, The primary cilium as the cell's antenna: Signaling at a sensory organelle. *Science* **313**, 629–633 (2006).
2. K. G. Kozminski, K. A. Johnson, P. Forscher, J. L. Rosenbaum, A motility in the eukaryotic flagellum unrelated to flagellar beating. *Proc. Natl. Acad. Sci.* **90**, 5519–5523 (1993).
3. B. Prevo, J. M. Scholey, E. J. G. Peterman, Intraflagellar transport: Mechanisms of motor action, cooperation, and cargo delivery. *FEBS J.* **284**, 2905–2931 (2017).
4. J. L. Rosenbaum, G. B. Witman, Intraflagellar transport. *Nat. Rev. Mol. Cell Biol.* **3**, 813–825 (2002).
5. J. J. Snow *et al.*, Two anterograde intraflagellar transport motors cooperate to build sensory cilia on C. elegans neurons. *Nat. Cell Biol.* **6**, 1109–1113 (2004).
6. L. A. Perkins, E. M. Hedgecock, J. N. Thomson, J. G. Culotti, Mutant sensory cilia in the nematode Caenorhabditis elegans. *Dev. Biol.* **117**, 456–487 (1986).
7. J. E. Evans *et al.*, Functional modulation of IFT kinesins extends the sensory repertoire of ciliated neurons in *Caenorhabditis elegans*. *J. Cell Biol.* **172**, 663–669 (2006).
8. D. Signor *et al.*, Role of a class DHC1b dynein in retrograde transport of IFT motors and IFT raft particles along cilia, but not dendrites, in chemosensory neurons of living *Caenorhabditis elegans*. *J. Cell Biol.* **147**, 519–530 (1999).

9. J. M. Scholey, Kinesin-2: A family of heterotrimeric and homodimeric motors with diverse intracellular transport functions. *Annu. Rev. Cell Dev. Biol.* **29**, 443–469 (2013).
10. D. G. Cole *et al.*, Novel heterotrimeric kinesin-related protein purified from sea urchin eggs. *Nature* **366**, 268–270 (1993).
11. D. G. Cole *et al.*, Chlamydomonas kinesin-II-dependent intraflagellar transport (IFT): IFT particles contain proteins required for ciliary assembly in Caenorhabditis elegans sensory neurons. *J. Cell Biol.* **141**, 993–1008 (1998).
12. Z. Walther, M. Vashishtha, J. L. Hall, The Chlamydomonas FLA10 gene encodes a novel kinesin-homologous protein. *J. Cell Biol.* **126**, 175–188 (1994).
13. K. G. Kozminski, P. L. Beech, J. L. Rosenbaum, The Chlamydomonas kinesin-like protein FLA10 is involved in motility associated with the flagellar membrane. *J. Cell Biol.* **131**, 1517–1527 (1995).
14. A. Chien *et al.*, Dynamics of the IFT machinery at the ciliary tip. *eLife* **6**, e28606 (2017).
15. B. D. Engel *et al.*, The role of retrograde intraflagellar transport in flagellar assembly, maintenance, and function. *J. Cell Biol.* **199**, 151–167 (2012).
16. X. Pan *et al.*, Mechanism of transport of IFT particles in *C. elegans* cilia by the concerted action of kinesin-II and OSM-3 motors. *J. Cell Biol.* **174**, 1035–1045 (2006).
17. G. Ou, O. E. Blacque, J. J. Snow, M. R. Leroux, J. M. Scholey, Functional coordination of intraflagellar transport motors. *Nature* **436**, 583–587 (2005).
18. B. Prevo, P. Mangeol, F. Oswald, J. M. Scholey, E. J. Peterman, Functional differentiation of cooperating kinesin-2 motors orchestrates cargo import and transport in *C. elegans* cilia. *Nat. Cell Biol.* **17**, 1536–1545 (2015).
19. J. Mijalkovic, B. Prevo, F. Oswald, P. Mangeol, E. J. Peterman, Ensemble and single-molecule dynamics of IFT dynein in *Caenorhabditis elegans* cilia. *Nat. Commun.* **8**, 14591 (2017).
20. H. Ishikawa, W. F. Marshall, Ciliogenesis: Building the cell's antenna. *Nat. Rev. Mol. Cell Biol.* **12**, 222–234 (2011).
21. T. A. Starich *et al.*, Mutations affecting the chemosensory neurons of *Caenorhabditis elegans*. *Genetics* **139**, 171–188 (1995).
22. L. B. Pedersen, J. L. Rosenbaum, Intraflagellar transport (IFT) role in ciliary assembly, resorption and signalling. *Curr. Top. Dev. Biol.* **85**, 23–61 (2008).
23. C. L. Williams *et al.*, Direct evidence for BBSome-associated intraflagellar transport reveals distinct properties of native mammalian cilia. *Nat. Commun.* **5**, 5813 (2014).
24. M. Taschner, E. Lorentzen, The intraflagellar transport machinery. *Cold Spring Harb. Perspect. Biol.* **8**, a028092 (2016).
25. C. Xie *et al.*, Optimal sidestepping of intraflagellar transport kinesins regulates structure and function of sensory cilia. *EMBO J.* **39**, e103955 (2020).
26. J. Mijalkovic, J. van Krugten, F. Oswald, S. Acar, E. J. Peterman, Single-molecule turnarounds of intraflagellar transport at the *C. elegans* ciliary tip. *Cell Rep.* **25**, 1701–1707.e1702 (2018).
27. G. J. Pazour, B. L. Dickert, G. B. Witman, The DHC1b (DHC2) isoform of cytoplasmic dynein is required for flagellar assembly. *J. Cell Biol.* **144**, 473–481 (1999).
28. K. P. Wedaman, D. W. Meyer, D. J. Rashid, D. G. Cole, J. M. Scholey, Sequence and submolecular localization of the 115-kD accessory subunit of the heterotrimeric kinesin-II (KRP85/95) complex. *J. Cell Biol.* **132**, 371–380 (1996).
29. J. C. Schafer, C. J. Haycraft, J. H. Thomas, B. K. Yoder, P. Swoboda, XBX-1 encodes a dynein light intermediate chain required for retrograde intraflagellar transport and cilia assembly in Caenorhabditis elegans. *Mol. Biol. Cell* **14**, 2057–2070 (2003).
30. B. P. Cormack, R. H. Valdivia, S. Falkow, FACS-optimized mutants of the green fluorescent protein (GFP). *Gene* **173**, 33–38 (1996).
31. N. C. Shaner *et al.*, Improved monomeric red, orange and yellow fluorescent proteins derived from Discosoma sp. red fluorescent protein. *Nat. Biotechnol.* **22**, 1567–1572 (2004).
32. J. Y. Tinevez *et al.*, TrackMate: An open and extensible platform for single-particle tracking. *Methods* **115**, 80–90 (2017).
33. P. Mangeol, B. Prevo, E. J. Peterman, KymographClear and KymographDirect: Two tools for the automated quantitative analysis of molecular and cellular dynamics using kymographs. *Mol. Biol. Cell* **27**, 1948–1957 (2016).
34. E. M. M. Manders, F. J. Verbeek, J. A. Aten, Measurement of co-localization of objects in dual-colour confocal images. *J. Microsc.* **169**, 375–382 (1993).
35. J. Schindelin *et al.*, Fiji: An open-source platform for biological-image analysis. *Nat. Methods* **9**, 676–682 (2012).
36. D. Arcizet, B. Meier, E. Sackmann, J. O. Rädler, D. Heinrich, Temporal analysis of active and passive transport in living cells. *Phys. Rev. Lett.* **101**, 248103 (2008).
37. H. Qian, M. P. Sheetz, E. L. Elson, Single particle tracking. Analysis of diffusion and flow in two-dimensional systems. *Biophys. J.* **60**, 910–921 (1991).
38. N. Tarantino *et al.*, TNF and IL-1 exhibit distinct ubiquitin requirements for inducing NEMO-IKK supramolecular structures. *J. Cell Biol.* **204**, 231–245 (2014).
39. M. J. Saxton, K. Jacobson, Single-particle tracking: Applications to membrane dynamics. *Annu. Rev. Biophys. Biomol. Struct.* **26**, 373–399 (1997).
40. N. Gal, D. Lechtman-Goldstein, D. Weihs, Particle tracking in living cells: A review of the mean square displacement method and beyond. *Rheol. Acta* **52**, 425–443 (2013).
41. D. Holcman *et al.*, Single particle trajectories reveal active endoplasmic reticulum luminal flow. *Nat. Cell Biol.* **20**, 1118–1125 (2018).
42. M. V. Nachury, E. S. Seeley, H. Jin, Trafficking to the ciliary membrane: How to get across the periciliary diffusion barrier? *Annu. Rev. Cell Dev. Biol.* **26**, 59–87 (2010).
43. N. B. Gilula, P. Satir, The ciliary necklace. A ciliary membrane specialization. *J. Cell Biol.* **53**, 494–509 (1972).
44. D. B. Doroquez, C. Berciu, J. R. Anderson, P. Sengupta, D. Nicastro, A high-resolution morphological and ultrastructural map of anterior sensory cilia and glia in Caenorhabditis elegans. *eLife* **3**, e01948 (2014).
45. F. Oswald, B. Prevo, S. Acar, E. J. G. Peterman, Interplay between ciliary ultrastructure and IFT-train dynamics revealed by single-molecule super-resolution imaging. *Cell Rep.* **25**, 224–235 (2018).
46. M. A. Jordan, D. R. Diener, L. Stepanek, G. Pigino, The cryo-EM structure of intraflagellar transport trains reveals how dynein is inactivated to ensure unidirectional anterograde movement in cilia. *Nat. Cell Biol.* **20**, 1250–1255 (2018).
47. K. Toropova *et al.*, Structure of the dynein-2 complex and its assembly with intraflagellar transport trains. *Nat. Struct. Mol. Biol.* **26**, 823–829 (2019).
48. L. Hostettler *et al.*, The bright fluorescent protein mneongreen facilitates protein expression analysis *in vivo. G3 (Bethesda)* **7**, 607–615 (2017).
49. F. Ye *et al.*, Single molecule imaging reveals a major role for diffusion in the exploration of ciliary space by signaling receptors. *eLife* **2**, e00654 (2013).
50. L. Milenkovic *et al.*, Single-molecule imaging of Hedgehog pathway protein Smoothened in primary cilia reveals binding events regulated by Patched1. *Proc. Natl. Acad. Sci. U.S.A.* **112**, 8320–8325 (2015).
51. L. E. Weiss, L. Milenkovic, J. Yoon, T. Stearns, W. E. Moerner, Motional dynamics of single Patched1 molecules in cilia are controlled by Hedgehog and cholesterol. *Proc. Natl. Acad. Sci. U.S.A.* **116**, 5550–5557 (2019).
52. W. Luo *et al.*, Axonemal lumen dominates cytosolic protein diffusion inside the primary cilium. *Sci. Rep.* **7**, 15793 (2017).
53. Y.-C. Lin *et al.*, Chemically inducible diffusion trap at cilia reveals molecular sieve-like barrier. *Nat. Chem. Biol.* **9**, 437–443 (2013).
54. N. L. Hendel, M. Thomson, W. F. Marshall, Diffusion as a ruler: Modeling kinesin diffusion as a length sensor for intraflagellar transport. *Biophys. J.* **114**, 663–674 (2018).
55. M. A. A. Mohamed, W. L. Stepp, Z. Ökten, Reconstitution reveals motor activation for intraflagellar transport. *Nature* **557**, 387–391 (2018).
56. M. Imanishi, N. F. Endres, A. Gennerich, R. D. Vale, Autoinhibition regulates the motility of the *C. elegans* intraflagellar transport motor OSM-3. *J. Cell Biol.* **174**, 931–937 (2006).
57. J. Burghoorn *et al.*, Mutation of the MAP kinase DYF-5 affects docking and undocking of kinesin-2 motors and reduces their speed in the cilia of *Caenorhabditis elegans*. *Proc. Natl. Acad. Sci. U.S.A.* **104**, 7157–7162 (2007).
58. P. Yi, C. Xie, G. Ou, The kinases male germ cell-associated kinase and cell cycle-related kinase regulate kinesin-2 motility in *Caenorhabditis elegans* neuronal cilia. *Traffic* **19**, 522–535 (2018).
59. P. Phirke *et al.*, Transcriptional profiling of C. elegans DAF-19 uncovers a ciliary base-associated protein and a CDK/CCRK/LF2p-related kinase required for intraflagellar transport. *Dev. Biol.* **357**, 235–247 (2011).
60. A. K. Maurya, T. Rogers, P. Sengupta, A CCRK and a MAK kinase modulate cilia branching and length via regulation of axonemal microtubule dynamics in *Caenorhabditis elegans*. *Curr. Biol.* **29**, 1286–1300.e1284 (2019).
61. C. Frøkjaer-Jensen *et al.*, Single-copy insertion of transgenes in *Caenorhabditis elegans*. *Nat. Genet.* **40**, 1375–1383 (2008).
62. S. Brenner, The genetics of *Caenorhabditis elegans*. *Genetics* **77**, 71–94 (1974).
63. I. Brust-Mascher, G. Ou, J. M. Scholey, Measuring rates of intraflagellar transport along *Caenorhabditis elegans* sensory cilia using fluorescence microscopy. *Meth. Enzymol.* **524**, 285–304 (2013).
64. A. G. Godin *et al.*, Single-nanotube tracking reveals the nanoscale organization of the extracellular space in the live brain. *Nat. Nanotechnol.* **12**, 238–243 (2017).